Hindawi
Advances in Materials Science and Engineering
Volume 2021, Article ID 5569091, 11 pages
https://doi.org/10.1155/2021/5569091

Research Article

Progressive Failure and Acoustic Emission Characteristics of Red Sandstone with Different Geometry Parallel Cracks under Uniaxial Compression Loading

Xizhen Sun,[1,2] **Fanbao Meng**,[2] **Ce Zhang**,[3] **Xucai Zhan**,[4] **and He Jiang**[4]

[1]*School of Civil Engineering and Architecture, Linyi University, Linyi 276000, China*
[2]*State Key Laboratory of Mining Disaster Prevention and Control, Shandong University of Science and Technology, Qingdao 266590, China*
[3]*Jinan Kingyue Highway Engineering Co. Ltd., Jinan 250101, China*
[4]*Qingdao Surveying and Mapping Research Institute, Qingdao 266032, China*

Correspondence should be addressed to Xizhen Sun; 496661950@qq.com and Fanbao Meng; mfbsdust@163.com

Received 22 January 2021; Revised 19 February 2021; Accepted 1 March 2021; Published 11 March 2021

Academic Editor: Xianjie Hao

The geometric distribution of initial damages has a great influence on the strength and progressive failure characteristics of the fractured rock mass. Initial damages of the fractured rock were simplified as parallel cracks in different geometric distributions, and then, the progressive failure and acoustic emission (AE) characteristics of specimens under the uniaxial compression loading were analyzed. The red sandstone (brittle materials) specimens with the parallel preexisting cracks by water jet were used in the tests. The energy peak and stress attenuation induced by the energy release of crack initiation were intuitively observed in the test process. Besides, three modes of rock bridge coalescence were obtained, and wing crack was the main crack propagation mode. The wing crack and other cracks were initiated in different loading stages, which were closely related to the energy level of crack initiation. The propagation of wing crack (stable crack) consumed a large amount of energy, and then, the propagation of shear crack, secondary crack, and anti-wing crack (unstable crack) was inhibited. The relationship between the crack propagation mode and the geometric distribution of existing cracks in the specimen was revealed. Meanwhile, the strength characteristic and failure mode of fractured rock with the different geometric distributions of preexisting crack were also investigated. The energy evolution characteristics and crack propagation were also analyzed by numerical modeling (PFC^{2D}).

1. Introduction

In underground engineering, rock mass as the main geological body has a lot of randomly distributed macroscopic and microscopic initial damages [1, 2]. The propagation and unstable failure of initial damage can induce engineering geological disasters under the mining influence [3–5]. The initial damage can be conceptualized as rock fracture in the laboratory, and the fracture instability characteristics and progressive failure of rock mass with different geometric distributions have a great significance for the prediction and control of fractured rock instability disasters [6].

In experimental tests, brittle rock-like materials with different crack geometric distribution are widely used, such as gypsum [7–11], concrete [12, 13], and glasses [14]. The crack angle, rock bridge mode, and crack distribution have been proved as the main factors affecting the crack initiation, propagation, and coalescence. However, artificial materials which have great differences with the initial rock materials are mainly used in these tests. The difference between artificial materials and initial rock leads to the diversity of the crack propagation.

Studies on the rock (sandstone, marble, etc.) fracture propagation were mainly performed under different loading modes. Zhang and Zhao [15] studied the fracture toughness and failure micromechanisms of marble under different loading rates. Yang et al. [16] and Wu et al. [17] investigated the crack propagation of sandstone with oval flaws and a

single hole under the uniaxial loading. Xu et al. [18] analyzed the compression-shear behaviors of brittle rocks under the static-dynamic loading by lab tests and numerical modeling. Zhou et al. [19] conducted the progressive cracking processes of granite with preexisting flaws. Vaneghi et al. [20] obtained the effects of loading amplitude and stress on the mechanical properties of sandstone and granodiorite. Li et al. [21] analyzed the dynamic strength and fracturing behavior of marble specimens with a single flaw. Hao et al. [22, 23] studied the time-dependent development of the excavation damaged zone (EDZ) around underground diversion tunnels in a columnar jointed rock mass and studied the fracture behaviour and crack propagation features of coal under coupled static-dynamic loading conditions. The single crack under the dynamic loading and tensile crack fatigue failure has been highlighted in most recent research of rock fracture propagation behaviors, while the complex crack propagation characteristics were rarely studied.

Red sandstone with preexisting cracks was used to simulate the parallel joints of the fractured rock mass. The fracture propagation tests of specimens with different geometric distributions under the uniaxial compression loading were conducted by the AG-X250 loading system and PCI-2 AE system. The energy evolution process was analyzed by PFC^{2D} numerical modeling. The progressive failure, AE characteristics, and energy evolution were obtained. Research results provide a reference for the prevention and control of rock mass instability under similar engineering conditions (uniaxial compression loading and parallel joints).

2. Specimen Preparation and Experimental Setup

2.1. Specimen Preparation. The size of the red sandstone specimen was 50 mm (width) × 22 mm (thickness) × 100 mm (length, L_1). The water jet cutting system was employed to obtain preexisting cracks, which were 20 mm in length (L_2) and 1 mm in aperture (A) (Yongda Dynamo Electric, Foshan, Guangzhou, China, as shown in Figure 1), and the angle with the horizontal direction was 45°, as shown in Figure 2. Three groups of specimens (three specimens in each group) were made with different geometric distributions. Table 1 lists the main parameters of red sandstone.

2.2. Loading and Monitoring System. The loading controlled mode (simulated the stress increase in underground engineering excavation) was set at an average loading rate of 0.05 kN/s by the AG-X250 loading system [25]. The crack propagation process was observed by using a high-speed video camera. In this test, the PCI-2 AE system (one Nano 30 sensor was used, as shown in Figure 3) was used to monitor the AE characteristics, and the couplant was applied between the sensors and the specimen surface to ensure the quality of the AE signal [11]. The AE parameters are shown in Table 2. The ambient noise and loading system noise were less than 30 dB (the threshold value was 40 dB). The AG-X250 loading system, PCI-2 AE system, and high-speed video camera (Figure 3) were used to collect data synchronously until the failure of specimens.

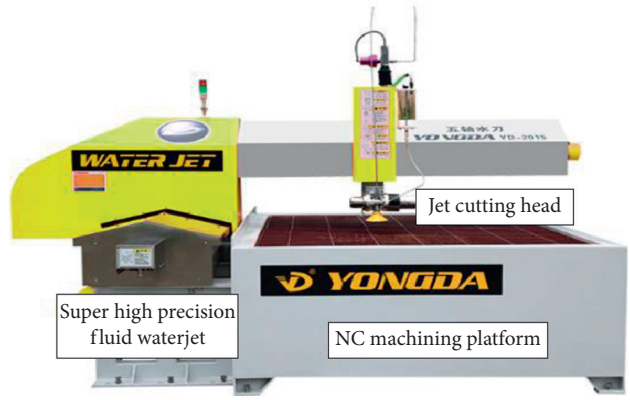

Figure 1: Water jet cutting system (the cutting accuracy and repetitive positioning accuracy were ±0.1 mm and ±0.05 mm, respectively; the working water pressure was less than 0.4 MPa).

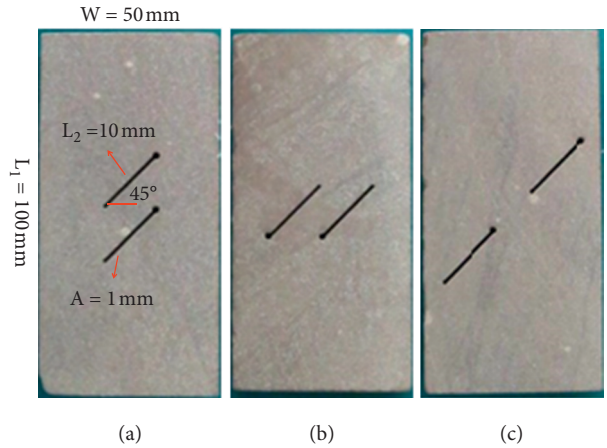

Figure 2: Red sandstone specimens with preexisting cracks: (a) Group 1; (b) Group 2; (c) Group 3.

3. Experimental Results and Discussion

3.1. Progressive Failure Laws. According to stress strain characteristics, the test process was divided into three stages: initial compression, elastic deformation, and peak failure, as shown in Figure 4. The crack propagation was concentrated in the peak failure stage. The wing crack of Group 1 and Group 3 was initiated in the elastic deformation stage (the wing crack of Group 2 was initiated near the peak stress), and axial stress decreased transitorily. The average stress of each group changed with geometry distributions. The average peak stress of Group 2 (15.11 MPa) was the lowest one, and that of Group 1 (23.12 MPa) was the highest one. Peak stress and their average are shown in Figure 5.

The homoplastic characteristics were observed in each group. Figures 6–8 show the typical progressive failure modes of these groups.

In this section, the preexisting crack was denoted by *pc*, wing crack by *wc*, shear cracks by *sc*, the mixed cracks (containing two crack modes: shear and tensile) by *mc*, the anti-wing crack by *ac*, the secondary crack (initiated from the newly generated cracks during the tests) by *sec*.

Table 1: The main parameters of red sandstone.

Density		2.40 g/cm^3
Material		Original brittle rock from Junan County, Linyi City, China
Particle sizes		0.07–0.30 mm [24]
Uniaxial compressive strength	77.95 MPa	Specimen size: 50 mm (diameter) × 100 mm (height)
Tangent elastic modulus	6.55 GPa	Uniaxial compression loading tests under the ISRM standard
Uniaxial tensile strength	3.76 MPa	Specimen size: 50 mm (diameter) × 25 mm (height) Brazilian disc test under the ISRM standard

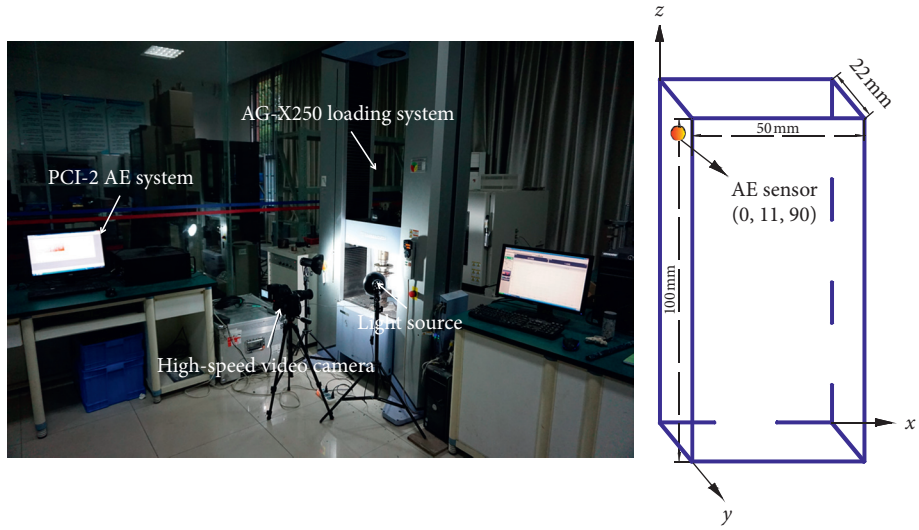

Figure 3: Loading and monitoring system.

Table 2: The AE parameters setup.

Resonant frequency	100–400 kHz
Sampling frequency	10^6 s
Threshold value	40 dB
Floating threshold value	5 dB

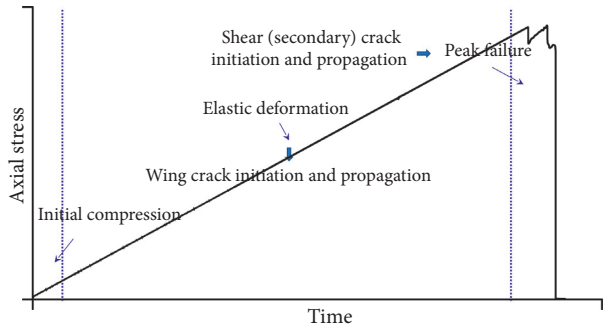

Figure 4: Three stages in the test process.

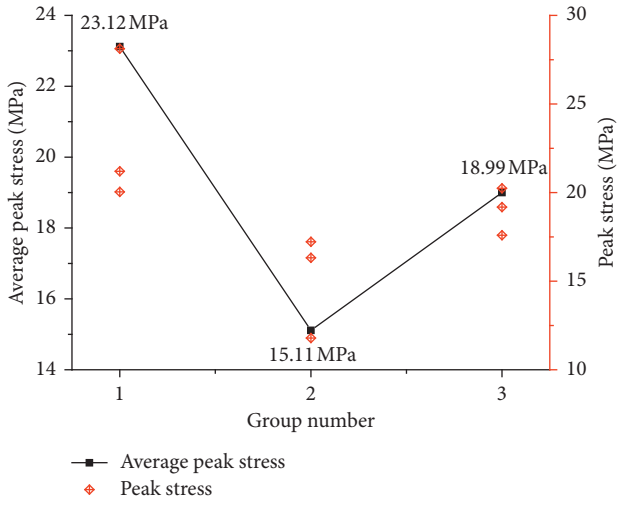

Figure 5: Peak stress and the average.

Figure 6 shows the progressive failure process of Group 1. When the first group of axial stress reached 8.55 MPa, wing cracks were initiated. At this time, the axial stress was reduced to 8.54 MPa. As the stress continued to increase to 20.70 MPa, mixed crack propagation resulted in the rock bridge coalescence. When the axial stress reached 28.12 MPa, the specimen was damaged.

Figure 7 shows the progressive failure process of Group 2. When the second group of axial stress reached 9.64 MPa, wing cracks were initiated with the rock bridge coalescence and anti-wing cracks were propagated simultaneously. The wing crack and secondary crack (initiated from the neonatal crack or the other part of preexisting crack except for the crack tip) were propagated when the stress was increased to 10.08 MPa. When the axial stress reached 11.79 MPa, the specimen was damaged.

Figure 8 shows the progressive failure process of Group 3. When the third group of axial stress reached 6.85 MPa, the wing cracks were initiated. The anti-wing crack was initiated

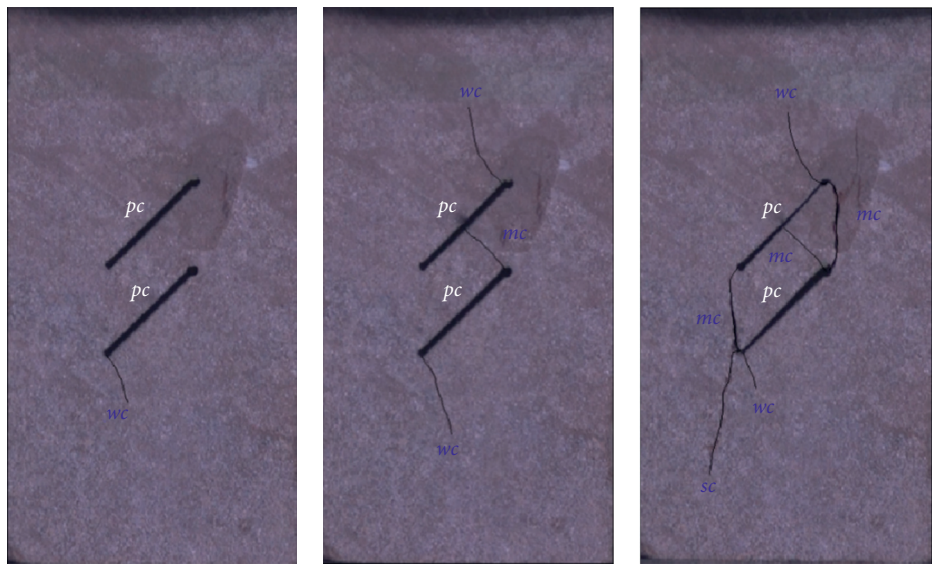

(a) (b) (c)

Figure 6: The progressive failure mode of Group 1: (a) 8.55 MPa; (b) 20.70 MPa; (c) 28.12 MPa.

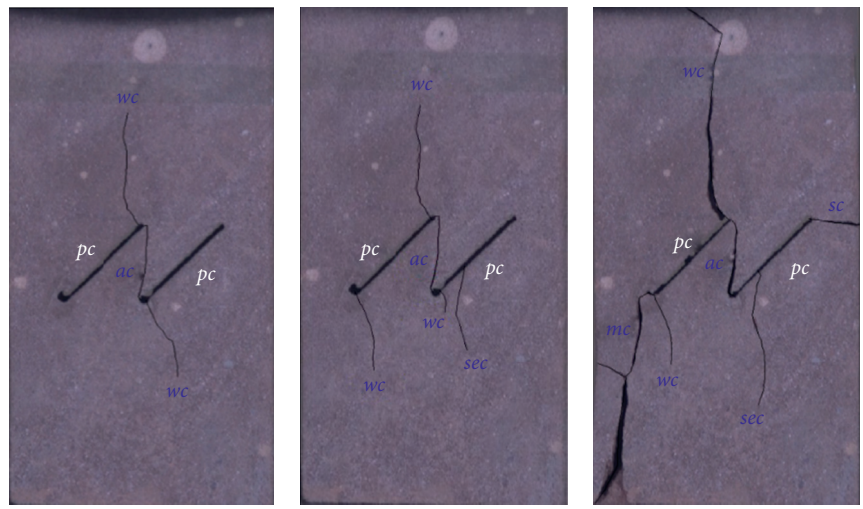

(a) (b) (c)

Figure 7: The progressive failure mode of Group 2: (a) 9.64 MPa; (b) 10.08 MPa; (c) 11.79 MPa.

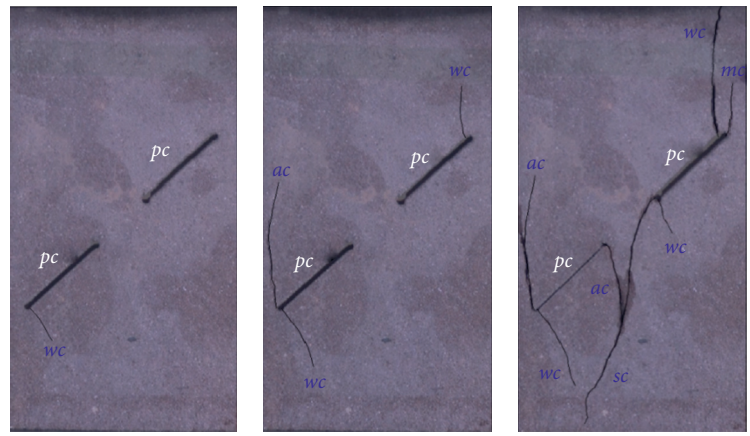

(a) (b) (c)

Figure 8: The progressive failure mode of Group 3: (a) 6.85 MPa; (b) 15.73 MPa; (c) 20.24 MPa.

when the stress was increased to 15.73 MPa. When the axial stress reached 20.24 MPa, the wing crack and anti-wing crack were propagated to the rock bridge coalescence, and the specimen was damaged.

The wing crack was the main propagation mode in the tests, accompanied by anti-wing crack, shear crack, secondary crack, and mixed crack. The wing crack as stable propagation mode was initiated primarily in the elastic deformation stage, and secondary crack and shear crack as unstable propagation modes were mostly initiated nearby the peak failure stage. Besides, there were three types of the rock bridge coalescence: mixed crack, anti-wing crack, and anti-wing crack-secondary crack.

3.2. AE Instability Characteristics. The AE phenomenon can reveal the microcrack propagation in the rock failure process, and it also was used as an effective way to investigate the rock fracture [26–28]. The AE parameters from the lab tests can be used as the key indexes for the disaster prevention and control of fractured rock mass instability [29]. The energy index which defined in the study of [4] was employed to investigate the instability characteristics in this test. Compared with other parameters (e.g., amplitude), the energy index can reflect the energy size of crack initiation and propagation effectively [30]. The coevolution law of energy index and axial stress was obtained in the crack propagation process.

The typical specimens with the different geometric distributions of preexisting cracks were analyzed under the uniaxial compression loading, as shown in Figure 9. When the wing crack of the specimen started to crack, the energy index of the three groups was 1670, 6940, and 108, respectively. At the same time, the stress of the first group of specimens decreased with crack initiation. When the rock bridge coalescence appeared, the energy index of the first and second group was 6050 and 6940. When the specimens were damaged, the energy index of three groups of specimens was 9380, 15353, and 11927, respectively.

Table 3 shows the stress and energy index of different crack modes. The energy was accumulated in the specimen internal during the loading process, and the energy was released during the crack initiation, rock bridge coalescence, and specimen failure, leading to the energy index peak and stress attenuation. The released energy was determined by the crack modes.

4. Numerical Modeling Tests and Analysis

The PFC^{2D} (version 5.0) was used to simulate the crack propagation characteristics [31–34]. The parameter calibration of numerical modeling was based on the uniaxial compressive test (ISRM standard), and the calibration results are shown in Figure 10. The number of particle ball was 10788, and the physical mechanical parameters are in Table 4.

The cohesive energy, strain energy, friction energy, kinetic energy, and boundary energy were analyzed in the numerical modeling process (other energy is negligible). The boundary energy was the energy on the model. The strain energy and cohesive energy were related to crack initiation and propagation. As the main energy mode, strain energy and cohesive energy increased with the deterioration degree of the model. The friction energy reacted after the crack initiation, and the friction effect was the main supplier of the residual strength. The kinetic energy was closely related to the dynamic equilibrium in the model.

The geometric distribution of cracks had a greater effect on energy parameters, as shown in Figure 11. The boundary energy, cohesive energy, and strain energy all increased gradually before the peak stress, however, the energy growth gradually decreased with the change of crack geometric distributions of specimens from Group 1 to Group 3. At the same time, the peak energy of specimens from Group 1 to Group 3 also decreased gradually. Before the peak stress, the kinetic energy and friction energy of the microparticles increased slowly. It indicated that the boundary energy before the peak stress was mainly provided by the cohesive energy and strain energy, and the energy supply of the samples with three geometric distributions was gradually weakened. Subsequently, the cohesive failure occurred, leading to an increase in friction between particles, especially the particles near the macrocracks. Meanwhile, the appearance of microcracks between particles weakened the coherence of particles, and the equilibrium of particle force was broken. The velocity of these particles increased gradually and the kinetic energy increased accordingly, even a few particles at the boundary of the model can completely break away from the bonding force and the model. After the peak stress, the cohesive energy and strain energy began to decrease, and the friction energy and kinetic energy began to increase rapidly.

The crack propagation modes obtained in numerical modeling were consistent with those in the laboratory tests. The preexisting crack tips were initiated due to the stress concentration. The tensile crack was the main crack mode, accompanied by shear crack, anti-wing crack, and secondary crack. However, the mechanism and material homogeneity between numerical modeling and laboratory tests had some differences, and the results varied in two conditions (laboratory tests and numerical modeling), as shown in Figure 12.

5. Discussion of Fracture Patterns

For specimens with the different geometric distributions of the preexisting cracks, the strength and propagation modes were extremely different in the lab tests and the PFC^{2D} (version 5.0) was used to simulate the crack propagation characteristics.

In the first group, the wing cracks and mixed crack initiation led to the stress attenuation and propagated stably, which rarely affected the strength of the specimens. The energy was consumed partially during the crack propagation process, preventing the premature coalescence of the rock bridge. The rock bridge coalesced in the peak failure stage, in which the axial strength was the highest. Besides, the crack propagation mode was relatively simple.

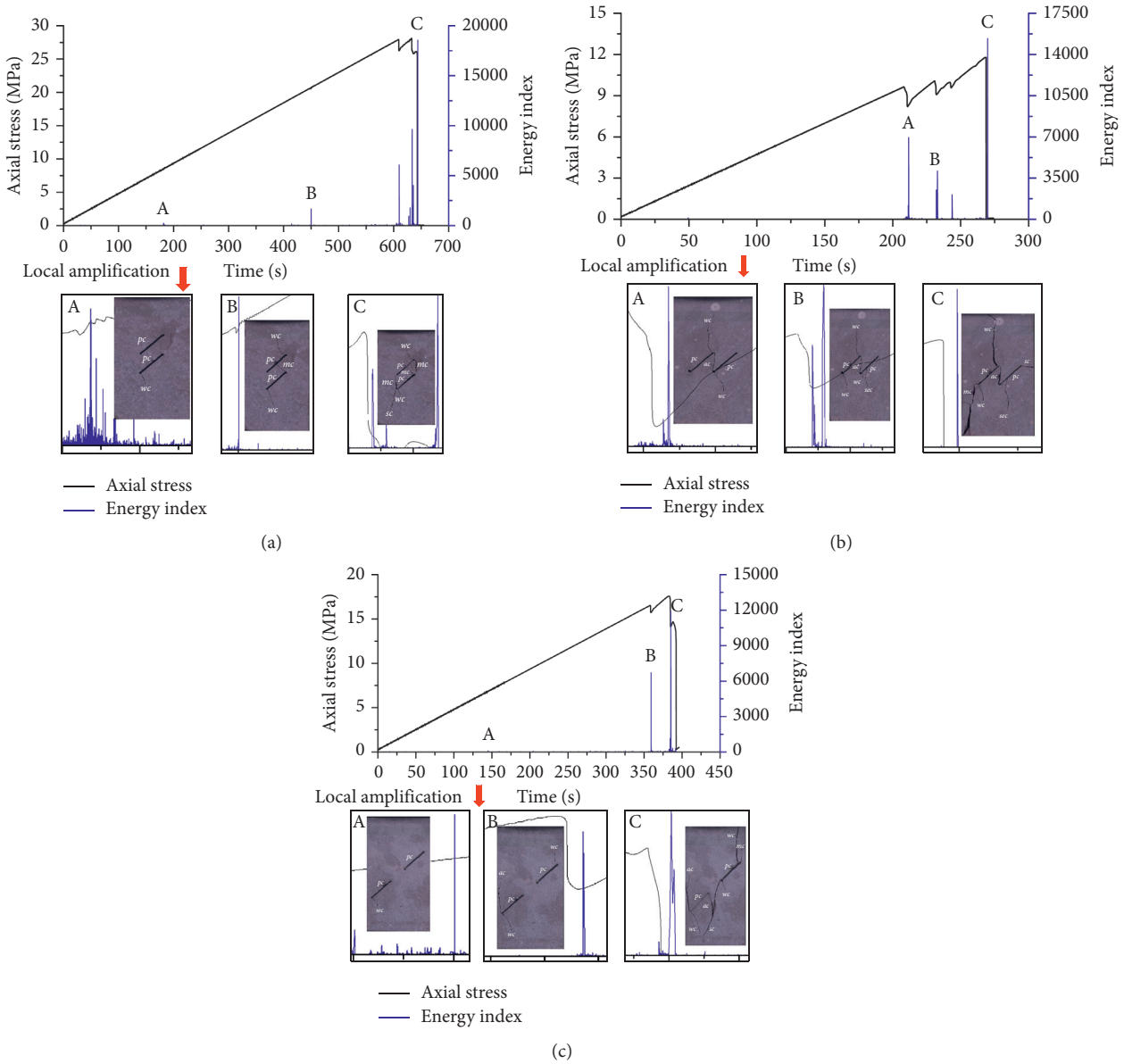

Figure 9: Results of the uniaxial compression loading test for red sandstone with the different geometric distributions: (a) Group 1; (b) Group 2; (c) Group 3.

Table 3: The stress and energy index of different crack modes.

Crack mode	Group 1	Group 2	Group 3	Parameters
Wing crack	8.55	9.64	6.85	Stress (MPa)
	1670	6940	108	Energy index
Rock bridge coalescence	20.70	9.64	—	Stress (MPa)
	6050	6940	—	Energy index
Specimen failure	28.12	11.79	20.24	Stress (MPa)
	9380	15353	11927	Energy index

In the second group, the wing cracks and anti-wing crack were initiated nearby peak stress, and their propagation led to the obvious stress attenuation. The specimen failure occurred after the propagation of wing cracks and anti-wing crack. In this group, the crack propagation mode was the most complicated; the rock bridge was more likely to coalesce, leading to the rapid failure of these specimens. Therefore, the strength was the minimum one.

In the third group, the preexisting cracks were propagated independently at the initial loading stage, and the wing cracks were initiated and propagated steadily. The consumed energy inhibited the initiation of anti-wing cracks and

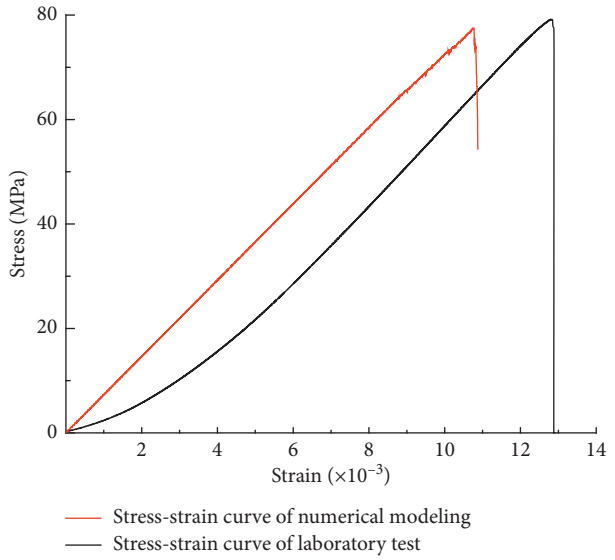

Figure 10: The calibration results between numerical modeling and laboratory test.

Table 4: Physico-mechanical parameters of red sandstone specimens.

Parameter	Value
Specimen size (H×D) (mm)	50×100
Particle diameter ratio (R_{min}/R_{max})	1
Stiffness ratio	1
Contact modulus of the particle (GPa)	1.60
Parallel bond deformation modulus (GPa)	1.60
Density ρ/Kg m^3	2500
Coefficient of friction	0.15
Particle contact damping	0.2
Bonding tensile strength/MPa	3.24
Parallel bond stiffness ratio	1

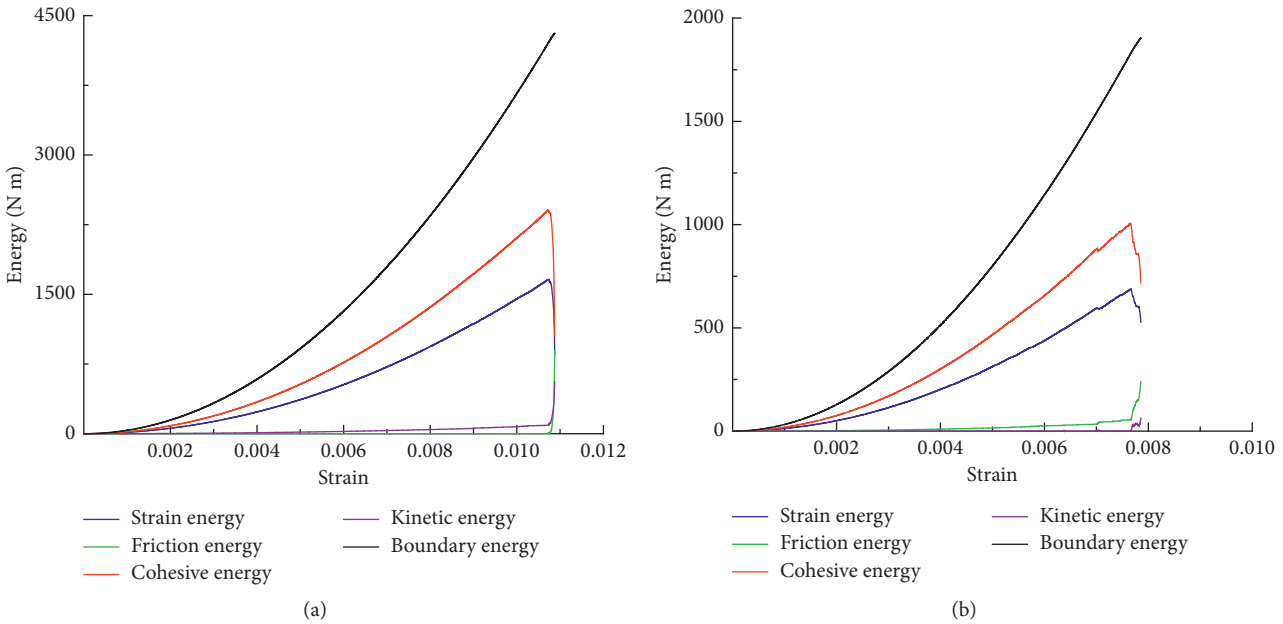

Figure 11: Continued.

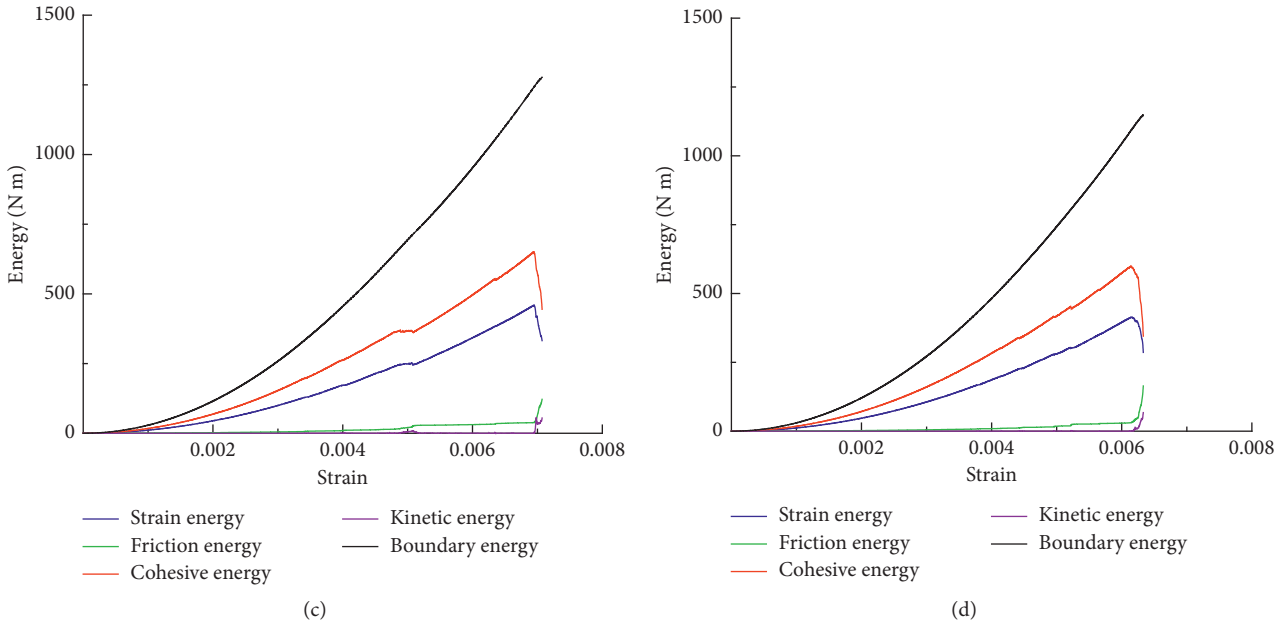

Figure 11: The energy evolution characteristics during numerical modeling process: (a) integrated specimen; (b) Group 1 specimen; (c) Group 2 specimen; (d) Group 3 specimen.

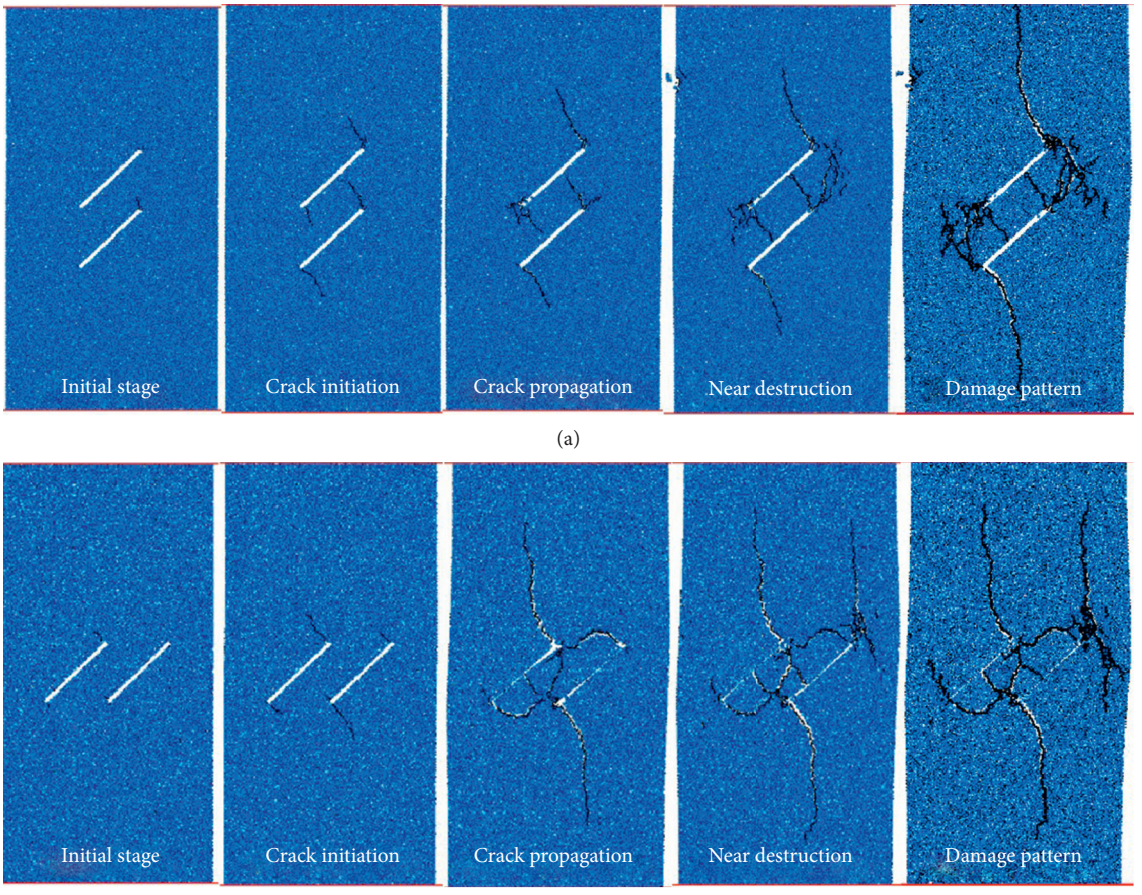

Figure 12: Continued.

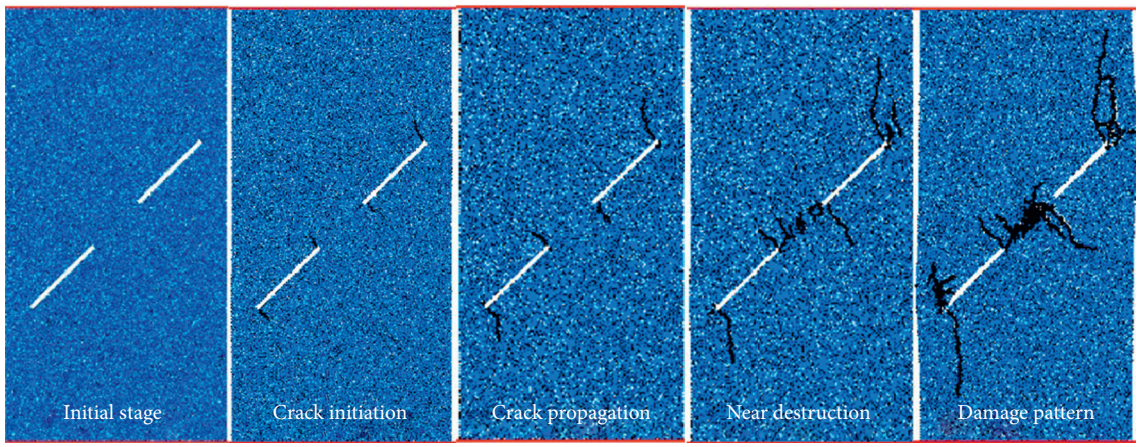

(c)

Figure 12: The crack propagation characteristics of the numerical modeling: (a) specimens in Group 1; (b) specimens in Group 2; (c) specimens in Group 3.

secondary cracks. The anti-wing cracks were initiated nearby the peak stress and greatly influenced the strength of the specimen. The propagation mode of specimens was relatively complicated.

The energy concentration occurred at the preexisting crack tips during the tests, and the initiation of wing crack occurred at the low or relatively low energy level. Therefore, the wing cracks were initiated and propagated steadily in the elastic deformation stage, and the strength of specimen was rarely affected. More energy was required for the initiation of anti-wing cracks and secondary cracks, and most of them were initiated nearby the peak stress. As a result, the rapid failure of specimens was caused. When the same energy was input, the energy level of shear crack initiation can be fleetly reached in the system without the dissipated energy of stable crack propagation. Therefore, the energy consumption of stable crack propagation restricted the unstable crack initiation to a certain extent, and the propagation mode and strength were changed with the different geometric distributions of cracks in specimens.

6. Conclusions

The crack propagation tests of red stone specimens with different geometric distributions were conducted under the uniaxial compression loading, and progressive failure laws and AE characteristics were investigated in lab tests. The conclusions are drawn as follows:

(1) The wing cracks are the main propagation mode, accompanied by the anti-wing cracks, mixed cracks, and secondary cracks. Three modes of rock bridge coalescence are observed: mixed crack (Group 1), anti-wing crack (Group 2), and anti-wing crack-secondary crack (Group 3). The energy is released by crack initiation and accumulated during the loading process, resulting in the energy index peak and the stress attenuation (the carrying capacity of the specimen decreases shortly). The energy level is determined by the crack propagation modes.

(2) The crack initiation and propagation include the following processes: energy concentration at the tip, crack initiation, and energy release. The energy released by wing crack initiation is lower than that by other cracks (anti-wing cracks, secondary cracks, and mixed cracks), and most of them are observed in the elastic deformation stage. Meanwhile, most of the other cracks are initiated in the peak failure stage, which is also determined by the energy level of crack initiation.

(3) The crack propagation modes are affected by the geometric distribution of preexisting crack in specimens. The difficulty of rock bridge coalescence and the stability of crack propagation are the key factors to determine the specimen strength and failure mode. The stable crack propagation consumes the energy and reduces the energy level, and the unstable crack initiation is inhibited partially. The crack propagation stability of specimens in Group 2 is the lowest, and the strength of specimens in Group 2 is the smallest.

(4) The results of PFC simulation results show that the boundary energy, cohesive energy, and strain energy of the specimen increase gradually with the loading before the peak stress, and the microcracks caused by cohesive failure are relatively few. A large number of particles are bonded and broken at the peak stress, and the movement and friction between particles increase gradually. After the peak stress, the cohesive energy and strain energy begin to decrease, and the friction energy and kinetic energy begin to increase rapidly.

Data Availability

The data used to support the findings of this study are available from the corresponding author upon request.

Conflicts of Interest

The authors declare that they have no conflicts of interest.

Acknowledgments

This study was supported by the National Natural Science Foundation of China (no. 51904149), the Shandong Provincial Natural Science Foundation, China (nos. ZR2019BEE013 and ZR2020QE129), the Open Foundation of Key Laboratory of Mining Disaster Prevention and Control (no. MDPC201910), and the Key Laboratory Open Foundation of Deep Coal Mine Excavation Response and Disaster Prevention and Control (no. KLDCMERDPC17108).

References

[1] S. Jiang, Y. Ye, X. Li et al., "DEM modeling of crack coalescence between two parallel flaws in SiC ceramics," *Ceramics International*, vol. 45, no. 12, pp. 14997–15014, 2019.

[2] Z. Wen, S. Jing, Y. Jiang et al., "Study of the fracture law of overlying strata under water based on the flow-stress-damage model," *Geofluids*, vol. 2019, no. 1, 12 pages, Article ID 3161852, 2019.

[3] X. Cai, Z. Zhou, L. Tan, H. Zang, and Z. Song, "Fracture behavior and damage mechanisms of sandstone subjected to wetting-drying cycles," *Engineering Fracture Mechanics*, vol. 234, p. 107109, 2020.

[4] X. Z. Sun, B. Shen, and B. L. Zhang, "Experimental study on propagation behavior of three-dimensional cracks influenced by intermediate principal stress," *Geomechanics and Engineering*, vol. 14, no. 2, pp. 195–202, 2018.

[5] Z. Zhou, X. Cai, X. Li, W. Cao, and X. Du, "Dynamic Response and energy evolution of sandstone under coupled static-dynamic compression: insights from experimental study into Deep rock engineering applications," *Rock Mechanics and Rock Engineering*, vol. 53, no. 3, pp. 1305–1331, 2020.

[6] Y. H. Huang and S. Q. Yang, "Particle flow simulation of macro- and meso-mechanical behavior of red sandstone containing two pre-existing non-coplanar fissures," *Chinese Journal of Rock Mechanics and Engineering*, vol. 33, no. 8, pp. 1644–1653, 2014.

[7] A. Bobet and H. H. Einstein, "Fracture coalescence in rock-type materials under uniaxial and biaxial compression," *International Journal of Rock Mechanics and Mining Sciences*, vol. 35, no. 7, pp. 863–888, 1998.

[8] A. Bobet, "The initiation of secondary cracks in compression," *Engineering Fracture Mechanics*, vol. 66, no. 2, pp. 187–219, 2000.

[9] L. N. Y. Wong and H. H. Einstein, "Crack coalescence in molded gypsum and carrara marble: part 1. macroscopic observations and interpretation," *Rock Mechanics and Rock Engineering*, vol. 42, no. 3, pp. 475–511, 2009.

[10] R. P. Janeiro and H. H. Einstein, "Experimental study of the cracking behavior of specimens containing inclusions (under uniaxial compression)," *International Journal of Fracture*, vol. 164, no. 1, pp. 83–102, 2010.

[11] X. Z. Sun, H. L. Wang, K. M. Liu, X. C. Zhan, and C. Y. Jia, "Experimental and numerical study on mixed crack propagation characteristics in rock-like material under uniaxial loading," *Geotechnical and Geological Engineering*, vol. 38, no. 1, pp. 191–199, 2019.

[12] Y. Zhao, L. Zhang, W. Wang, C. Pu, W. Wan, and J. Tang, "Cracking and stress-strain behavior of rock-like material containing two flaws under uniaxial compression," *Rock Mechanics and Rock Engineering*, vol. 49, no. 7, pp. 2665–2687, 2016.

[13] P. Cao, T. Liu, C. Pu, and H. Lin, "Crack propagation and coalescence of brittle rock-like specimens with pre-existing cracks in compression," *Engineering Geology*, vol. 187, pp. 113–121, 2015.

[14] E. Hoek and Z. T. Bieniawski, "Brittle fracture propagation in rock under compression," *International Journal of Fracture Mechanics*, vol. 1, no. 3, pp. 137–155, 1965.

[15] Q. B. Zhang and J. Zhao, "Effect of loading rate on fracture toughness and failure micromechanisms in marble," *Engineering Fracture Mechanics*, vol. 102, pp. 288–309, 2013.

[16] S.-Q. Yang, Y.-H. Huang, W.-L. Tian, and J.-B. Zhu, "An experimental investigation on strength, deformation and crack evolution behavior of sandstone containing two oval flaws under uniaxial compression," *Engineering Geology*, vol. 217, pp. 35–48, 2017.

[17] H. Wu, G. Zhao, W. Liang, E. Wang, and S. Ma, "Experimental investigation on fracture evolution in sandstone containing an intersecting hole under compression using DIC technique," *Advances in Civil Engineering*, vol. 2019, Article ID 3561395, 12 pages, 2019.

[18] Y. Xu, F. Dai, and H. B. Du, "Experimental and numerical studies on compression-shear behaviors of brittle rocks subjected to combined static-dynamic loading," *International Journal of Mechanical Sciences*, vol. 175, 2020.

[19] X.-P. Zhou, J.-Z. Zhang, Q.-H. Qian, and Y. Niu, "Experimental investigation of progressive cracking processes in granite under uniaxial loading using digital imaging and AE techniques," *Journal of Structural Geology*, vol. 126, pp. 129–145, 2019.

[20] R. G. Vaneghi, B. Ferdosi, A. D. Okoth et al., "Strength degradation of sandstone and granodiorite under uniaxial cyclic loading," *Journal of Rock Mechanics and Geotechnical Engineering*, vol. 10, pp. 117–126, 2018.

[21] X. Li, T. Zhou, and D. Li, "Dynamic strength and fracturing behavior of single-flawed prismatic marble specimens under impact loading with a split-hopkinson pressure bar," *Rock Mechanics and Rock Engineering*, vol. 50, no. 1, pp. 29–44, 2017.

[22] X. Hao, W. Du, Y. Zhao et al., "Dynamic tensile behaviour and crack propagation of coal under coupled static-dynamic loading," *International Journal of Mining Science and Technology*, vol. 30, no. 5, pp. 659–668, 2020.

[23] X.-J. Hao, X.-T. Feng, C.-X. Yang, Q. Jiang, and S.-J. Li, "Analysis of EDZ development of columnar jointed rock mass in the baihetan diversion tunnel," *Rock Mechanics and Rock Engineering*, vol. 49, no. 4, pp. 1289–1312, 2016.

[24] S. J. Chen, Y. H. Guo, W. P. Huang et al., "Experimental study of influence regularity and mechanism of particle size on mechanical properties of red sandstone," *Journal of Shandong University of Science and Technology (Natural Science)*, vol. 36, pp. 8–14, 2017.

[25] D. W. Yin, S. J. Chen, W. B. Xing et al., "Experimental study on mechanical behavior of roof-coal pillar structure body under different loading rates," *Journal of China Coal Society*, vol. 43, no. 5, pp. 1249–1257, 2018.

[26] G. Shi, X. Yang, H. Yu, and C. Zhu, "Acoustic emission characteristics of creep fracture evolution in double-fracture fine sandstone under uniaxial compression," *Engineering Fracture Mechanics*, vol. 210, pp. 13–28, 2019.

[27] A. Cao, G. Jing, Y.-l. Ding, and S. Liu, "Mining-induced static and dynamic loading rate effect on rock damage and acoustic

emission characteristic under uniaxial compression," *Safety Science*, vol. 116, pp. 86–96, 2019.

[28] P. Rodríguez and T. B. Celestino, "Application of acoustic emission monitoring and signal analysis to the qualitative and quantitative characterization of the fracturing process in rocks," *Engineering Fracture Mechanics*, vol. 210, pp. 54–69, 2019.

[29] X.-T. Feng, Y.-Y. Zhou, and Q. Jiang, "Rock mechanics contributions to recent hydroelectric developments in China," *Journal of Rock Mechanics and Geotechnical Engineering*, vol. 11, no. 3, pp. 511–526, 2019.

[30] X. J. Hao, Y. N. Wei, K. Yang et al., "Anisotropy of crack initiation strength and damage strength of coal reservoirs," *Petrol Explor Dev+*, vol. 48, no. 1, pp. 1–12, 2021.

[31] X. Wang and L. G. Tian, "Mechanical and crack evolution characteristics of coal-rock under different fracture-hole conditions: a numerical study based on particle flow code," *Environmental Earth Science*, vol. 77, p. 297, 2018.

[32] Itasca Consulting Group Inc, *PFC (Particle Flow Code)*, ICG, Minneapolis, MN, USA, 2014.

[33] P. A. Cundall and O. D. L. Strack, "A discrete numerical model for granular assemblies," *Géotechnique*, vol. 29, no. 1, pp. 47–65, 1979.

[34] X. Wang, Z. Wen, Y. Jiang, and H. Huang, "Experimental study on mechanical and acoustic emission characteristics of rock-like material under non-uniformly distributed loads," *Rock Mechanics and Rock Engineering*, vol. 51, no. 3, pp. 729–745, 2018.